J. Fluid Mech. (1994), *vol.* 280, *pp.* 349–368

Topographic Hadley cells

By S. A. CONDIE† AND P. B. RHINES

School of Oceanography WB-10, University of Washington, Seattle, WA 98195, USA

(Received 7 July 1993 and in revised form 9 June)

When a rotating fluid over sloping topography is heated from below and/or cooled from above, horizontal temperature gradients develop which drive convection cells aligned with isobaths. We refer to these cells as *topographic Hadley cells*. Laboratory experiments reveal that sinking occurs in small cyclonic vortices situated in relatively shallow regions. This is balanced by slower upwelling in adjacent deeper regions. The cross-isobath motions which connect the upwelling and downwelling are accelerated by Coriolis forces, resulting in strong jets which follow isobathic contours. For anti-clockwise rotation, the surface jets keep the shallows to their left when looking in the direction of flow, which is opposite to both Kelvin and Rossby wave propagation. The width of the jets scales with the Rossby deformation radius and if this is much less than the width of the slope region then a number of parallel jets form. Motions on the deeper side of the jets where the flow is accelerating are adequately described by linear inviscid theory. However, the strong shears generated by this acceleration lead to baroclinic instability. The resulting cross-stream momentum fluxes broaden and flatten the velocity profile, allowing the flow on the shallow side of the jet to decelerate smoothly before sinking. Topographic Hadley cells are dynamically similar to terrestrial atmospheric Hadley cells and may also be relevant to the zonal jet motions observed on Jupiter and Saturn. It is also suggested that in coastal seas they may represent an important mode of heat (or salt) transfer where surface cooling (or evaporation) drives convection.

1. Introduction

If a fluid of varying depth is uniformly cooled from above, the coldest fluid will be produced in shallow regions owing to the smaller heat capacity per unit area. The flow responds to the cross-isobath temperature gradient by establishing convection cells, characterized by downwelling in shallows balanced by upwelling in deeper regions. In an inertial reference frame there is no along-isobath component. However, if the fluid is also rotating, the horizontal motions within the cell will be accelerated in the along-isobathic direction by Coriolis forces. This is illustrated schematically in figure 1. As relatively warm fluid nears the free surface and begins to move toward the shallows, it is accelerated to the right (anti-clockwise rotation), thus forming an along-isobath jet which keeps the shallows to its left. The bottom flow will similarly form a jet in the opposite direction, although this may be significantly weakened by dissipation in the bottom Ekman layer. Because of a close dynamical analogy between the formation of zonal jets over topography and the formation of the jet

† Present address: Research School of Earth Sciences, The Australian National University, Canberra, ACT 0200, Australia.

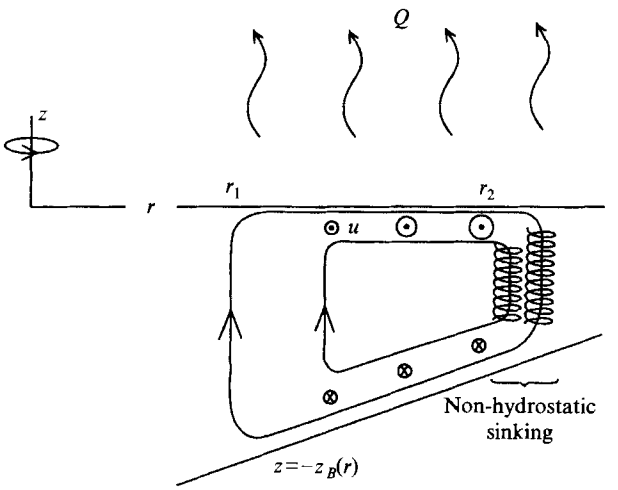

FIGURE 1. Schematic representation of the convection cell. Without rotation the azimuthal velocity is zero and a single radially overturning cell covers the entire slope region. The addition of rotation causes the horizontal motions to accelerate in the azimuthal direction (normal to the page) and limits the width of the cell.

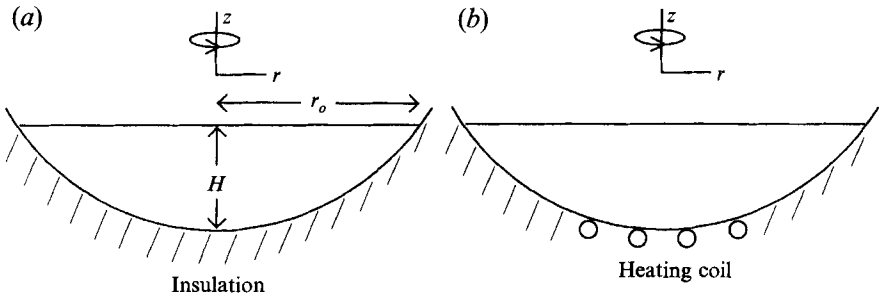

FIGURE 2. Experimental configurations for (*a*) flows with an insulated perspex bottom and (*b*) flows with a heated aluminium bottom. The bowls were spherical in shape with spherical radii of 22 cm and 30 cm for (*a*) and 22 cm for (*b*). The smaller bowls were typically filled to a depth of $H = 7.5$ cm giving a free surface radius of $r_o = 17$ cm, while for the larger bowl $H = 11$ cm and $r_o = 23$ cm.

stream by the atmospheric Hadley cell, we refer to the convection cells as *topographic Hadley cells.*

The convection cells can be readily produced in laboratory experiments by allowing water in a thermally insulated rotating bowl to cool at the free surface (figure 2). In figure 3 the surface flow is visualized by a streak photograph of floating aluminium powder. It is characterized by at least two highly unstable clockwise jets, separated by rings of small cyclonic (anti-clockwise) vortices. The vortices form the downwelling component of the convection cells, carrying cooled surface water downward in spiralling motions to the bottom. These structures are similar to those observed in rotating Bénard convection experiments over a flat bottom (Boubnov & Golitsyn 1986; Chen, Fernando & Boyer 1989; Fernando, Chen & Boyer 1991). Without topography, downwelling in cyclonic vortices is surrounded by anticyclonic upwelling motions. However, with the addition of topography as in figure 3, upwelling occurs in adjacent deeper regions where it generates the azimuthal jets.

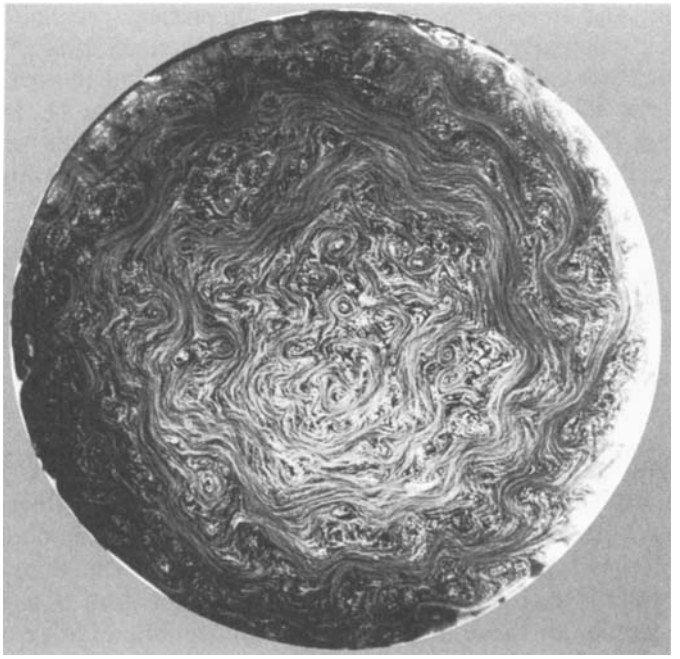

FIGURE 3. A streak photograph of surface particles in the large insulated bowl (figure 2*a*) containing water cooled from above. The fluid radius was $r_o = 23$ cm at the free surface and the maximum fluid depth was 11 cm. The rotation rate corresponded to $f = 1.4\ \mathrm{s}^{-1}$ and the temperature difference between the air and water was 12°C.

The flows described in this study have some features in common with those produced by imposing radial temperature gradients along horizontal boundaries. Koschmieder & Lewis (1986) observed Hadley circulations over a rotating plate with radial temperature gradients and an isothermal lid. Some experiments were conducted with unstable vertical gradients, but were restricted to relatively low rotation rates. Miller & Fowlis (1986) and Hathaway & Fowlis (1986) imposed gradients along both the top and bottom boundaries, over a wider parameter range including unstable vertical gradients. One obvious difference in our study is the use of topography to generate the horizontal temperature gradients. However, an equally important variation is the use here of a free surface. In the previous studies most of the radial heat transfer was concentrated within Ekman boundary layers and extended over the full radius of the container, whereas our surface flow is predominantly inertial so that the internal dynamics determine both the width of the cells and the heat flux through the free surface. While such a system allows fewer parameters to be set externally, it should be more relevant to meteorological and oceanographic phenomena. For example, the atmospheric Hadley cell does not extend from equator to pole, but is restricted to lower latitudes by its internal dynamics.

2. The linear inviscid limit

It is clear from figure 3 that nonlinearity has a significant influence on topographic Hadley cells. However, the linear inviscid limit is analytically tractable and will help provide physical insight into the more complex laboratory flows. The dynamics of

the convective vortices which form the downwelling arm of the topographic Hadley cells are turbulent and non-hydrostatic, making theoretical progress beyond linear stability analysis particularly difficult (Nakagawa & Frenzen 1955; Chandrasekhar 1961). We will therefore treat this part of the flow as a conduit removing cooled fluid from the top of the cell and returning it near the base (figure 1). In contrast, the jet regions are less thermodynamically active and are likely to be near hydrostatic balance. Nonlinearity can also be neglected if the Rossby number satisfies

$$Ro = \frac{u}{f\Delta r} \ll 1, \tag{2.1}$$

where u is the azimuthal jet velocity, Δr is the jet width and f is the Coriolis parameter which in the laboratory is equal to twice the rotation rate. Similarly, if the Ekman number satisfies

$$Ek = \frac{\nu}{fH^2} \ll 1, \tag{2.2}$$

where ν is the kinematic viscosity and H is the fluid depth, then dissipation will be small outside the bottom Ekman layer. Under these conditions the jets will be dominated by a geostrophic balance in the cross-stream direction, so that the thermal wind relation holds (Pedlosky 1987, pp. 42–46). The final assumption is that the surface flow is inviscid so that its angular momentum is conserved. These assumptions are similar to those utilized in the atmospheric Hadley cell solution of Held & Hou (1980). They will now be utilized in a theory which predicts the free surface velocity distribution, the depth-averaged density distribution and the size of the hydrostatic region of an idealized linear inviscid cell.

Consider the hydrostatic region of the cell in figure 1, with no gradients in the azimuthal direction. The cross-isobath (r) momentum balance is geostrophic,

$$-fu = -\frac{1}{\rho_0}\frac{\partial p}{\partial r}, \tag{2.3}$$

while the vertical (z) momentum equation for hydrostatic Bousinesq flow is

$$0 = -\frac{1}{\rho}\frac{\partial p}{\partial z} - g. \tag{2.4}$$

Here, $p(r,z)$ is the pressure, $\rho(r,z)$ is the density with a mean value ρ_o, and g is the gravitational acceleration.

The specific angular momentum of fluid particles is defined by

$$M = \tfrac{1}{2}fr^2 + ur. \tag{2.5}$$

If the cell extends radially from $r = r_1$ to $r = r_2$, then conservation of M implies immediately that the surface velocity is

$$u(r,0) = \frac{fr_1}{2}\left(\frac{r_1}{r} - \frac{r}{r_1}\right). \tag{2.6}$$

This constraint does not apply to the bottom boundary $z = -z_B(r)$, where we assume

$$u(r,-z_B) \ll u(r,0). \tag{2.7}$$

The surface velocity is plotted as a function of position in figure 4. Warm fluid surfaces at $r = r_1$, then accelerates with the shallows to its left until it sinks at $r = r_2$

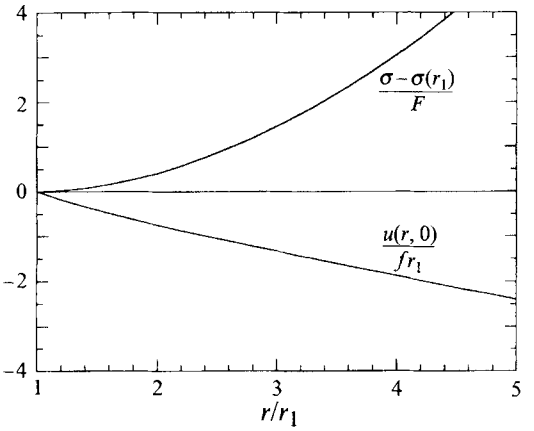

FIGURE 4. Non-dimensional zonal velocity and depth-averaged density anomaly as a function of cross-cell coordinate. The fluid depth decreases with increasing r and the theoretical curves only apply over the width of the hydrostatic region of each cell (to be determined).

where the maximum azimuthal speed is

$$u_{max} = \mid u(r_2, 0) \mid = f\Delta r \left(1 - \frac{\Delta r}{2r_2}\right), \tag{2.8}$$

with $\Delta r = r_2 - r_1$. Beyond r_2, equation (2.6) no longer applies and in the inviscid limit the velocity can be assumed to drop discontinuously to zero. However, a fluid of finite viscosity clearly cannot support an infinite shear. Since Rossby numbers based on u_{max} can approach unity, it is likely that the shear will be reduced by nonlinear momentum fluxes which would tend to broaden and flatten the velocity profile. While these effects cannot be included in the analytical theory, they will be investigated in the laboratory component of the study.

Eliminating the pressure term from (2.3) and (2.4) to produce the thermal wind equation, then integrating from the bottom $z = -z_B(r)$ to the free surface $z = 0$, yields

$$f\{u(r,0) - u(r,-z_B)\} = -gH\frac{\partial \sigma}{\partial r}, \tag{2.9}$$

where g is the gravitational acceleration, H is the characteristic depth of the cell and the non-dimensional depth-averaged density distribution is defined by

$$\sigma(r) = \frac{1}{\rho_o H}\int_{-z_B}^{0} \rho \mathrm{d}z. \tag{2.10}$$

Since ρ_o is the mean density of the cell,

$$\int_{r_1}^{r_2} \sigma \mathrm{d}r = \Delta r. \tag{2.11}$$

Utilizing boundary conditions (2.6) and (2.7) in relation (2.9), then integrating from r_1 to r yields an expression for the depth-averaged density distribution,

$$\sigma(r) = \sigma(r_1) + \frac{F_1}{4}\left\{\left(\frac{r}{r_1}\right)^2 - 2\ln\left(\frac{r}{r_1}\right) - 1\right\}, \tag{2.12}$$

where $F_1 = f^2 r_1^2 / g\overline{H}$ is a Froude number based on r_1. The density distribution is plotted as a function of position in figure 4. The density increases with decreasing r until sinking occurs at a critical density $\sigma(r_2)$. If the density change across the cell is defined as $\Delta\sigma = \sigma(r_2) - \sigma(r_1)$, then equation (2.12) gives,

$$\Delta\sigma = \frac{F_1}{4}\left\{\left(\frac{\Delta r}{r_1}\right)^2 - 2\ln\left(1 + \frac{\Delta r}{r_1}\right) + 2\frac{\Delta r}{r_1}\right\}, \tag{2.13}$$

where we have substituted $r_2 = r_1 + \Delta r$. The power series expansion

$$\ln\left(1 + \frac{\Delta r}{r_1}\right) = \frac{\Delta r}{r_1}\left\{1 - \frac{1}{2}\frac{\Delta r}{r_1} + O\left(\frac{\Delta r^2}{r_1^2}\right)\right\}, \tag{2.14}$$

when substituted into (2.13) yields

$$\frac{\Delta r}{r_1} = \left(\frac{2\Delta\sigma}{F_1}\right)^{1/2} \tag{2.15}$$

for $\Delta r^2 / r_1^2 \ll 1$. If $\Delta r^2 / r_1^2 \gg 1$, the first term on the right-hand side of (2.13) dominates and the jet width is larger than (2.15) by a factor of $\sqrt{2}$.

To close the problem, $\Delta\sigma$ must now be related to external variables. This can be achieved by equating the vertical heat flux through the water with that through the air above it. In each of these fluids the vertical heat flux Q obeys

$$Q \sim \left(\frac{k\Delta T}{H}\right) Ra^{1/3} \tag{2.16}$$

(Turner 1973, pp. 219–224), where ΔT is the change in temperature across the layer (concentrated in the thermal boundary layer), k is the thermal conductivity of the medium and evaporative cooling has been neglected. The Rayleigh number (assumed to be large) is defined by

$$Ra = \frac{g\alpha\Delta T H^3}{\kappa\nu}, \tag{2.17}$$

where α is the coefficient of thermal expansion, κ is the thermal diffusivity and ν is the kinematic viscosity. For cooling at a free surface, the vertical heat flux through the water must equate with that through the air above it. It then follows from (2.16) that the ratio of the temperature change across the water to that across the air is

$$\gamma = \left\{\left(\frac{k'}{k}\right)^3 \frac{\alpha'\kappa\nu}{\alpha\kappa'\nu'}\right\}^{1/4}, \tag{2.18}$$

where primed quantities refer to the properties of air and unprimed to the properties of water. Over the experimental parameter range $\gamma = 0.03$, implying that nearly all the temperature drop is across the air thermal boundary layer. The drop across the water can then be approximated by $\gamma\Delta T$, where ΔT now denotes the total temperature difference between the air and water. Since the convective overturning timescales for the cell are much shorter than diffusive timescales, the vertical and horizontal temperature changes across the cell should be very similar. A reasonable approximation for the density change across the cell is therefore

$$\Delta\sigma = \gamma\alpha\Delta T. \tag{2.19}$$

With $\gamma = 0.03$, the change in temperature across the cell is only a few percent of ΔT.

It then follows from (2.16) and (2.17) that horizontal gradients in Q will also be very small.

Substituting (2.19) into (2.15) gives width scales of

$$\Delta r = (2\gamma)^{1/2}R \qquad (\Delta r^2 \ll r_1^2) \tag{2.20}$$

and

$$\Delta r = 2\gamma^{1/2}R \qquad (\Delta r^2 \gg r_1^2), \tag{2.21}$$

where

$$R = \frac{(g\alpha\Delta T H)^{1/2}}{f} \tag{2.22}$$

is a deformation radius based on external parameters. Since $\Delta r \gg r_1$ implies $\Delta r \approx r_2$, relation (2.8) provides corresponding scales for the maximum surface speed,

$$u_{max} = (2\gamma)^{1/2} fR \qquad (\Delta r^2 \ll r_1^2) \tag{2.23}$$

and

$$u_{max} = \gamma^{1/2} fR \qquad (\Delta r^2 \gg r_1^2). \tag{2.24}$$

Scales (2.21) and (2.24) break down for very broad jets in which Δr approaches the container radius r_o. Validity of the theory is therefore restricted to the regime

$$Fr = \frac{r_o^2}{R^2} \gg 1, \tag{2.25}$$

where Fr is a Froude number.

It is interesting to note that the theoretical results do not depend directly on the details of the topography. The only requirement is that the bottom slope is large enough to generate the required cross-slope temperature gradients in the fluid (see the Appendix). Similar results would therefore be obtained if the same gradients could be applied by other methods. However, it is essential that the upper boundary be a free surface. Limitation of the cell width to the deformation radius scale is a direct consequence of angular momentum conservation of the near surface flow. Introduction of a solid upper boundary, as in the laboratory experiments of Koschmieder & Lewis (1986), Miller & Fowlis (1986) and Hathaway & Fowlis (1986), enhances dissipation and breaks the angular momentum constraint. In the extreme case where the Ekman layer carries all of the radial transport V_E, the cell will extend over the full width of the container and the azimuthal velocity will scale as

$$u \sim V_E(f/\nu)^{1/2} \tag{2.26}$$

(Pedlosky 1987, p. 192).

3. Laboratory results

Two experimental configurations were used to study topographic Hadley cells. The simplest consisted of an insulated perspex bowl mounted on a rotating table (figure 2*a*). This was filled with water ranging from 10 to 35°C above the laboratory temperature which was fixed at 20°C. Cooling at the free surface then forced a convective flow in the bowl. Since there was no heating, this flow was inherently unsteady. However, the convective overturning timescale was always much less than the cooling timescale, so that the flow could be regarded as quasi-steady. In the second series of experiments, a rotating aluminium bowl containing the fluid was heated from

below by a thermostatically controlled electric element attached to the bottom of the bowl (figure 2*b*). This was balanced by cooling at the free surface, so that a steady mean state could be established in these runs. Under these circumstances, ΔT was defined as twice the mean temperature difference between the air and water. The heating element was restricted to the deepest part of the bowl, so that the heat flux distribution would enhance the radial gradients generated by the topography. The experiments seem to confirm that it is the magnitude of the forcing rather than its detailed spatial structure which determines the flow patterns in this configuration.

In both series of experiments, the free surface flow was visualized using floating aluminium powder or polystyrene beads. Streak photographs and video recordings then provided information on the general flow patterns and the surface velocity field. The temperature structure was also measured by traversing fast response thermistors both vertically and horizontally through the flow. A small number of experiments involved cooling through a solid upper boundary and in these cases, interior velocity measurements were made using a laser Doppler velocimeter (LDV).

The important parameters which characterize the rotating bowl experiments are f, ΔT, ν, κ, H and r_o, where the last two quantities can be interpreted as the depth at the bowl centre and the radius where the depth goes to zero (figure 2). The system can therefore be defined in terms of four non-dimensional parameters (*Ra*, *Fr*, *Ek* and say a Prandtl number, $Pr = \nu/\kappa$). However, since all of the current experiments utilized pure water, ν and κ are essentially constant and it is only necessary to specify two parameters (say *Ra* and *Fr*). All of the experiments described below were characterized by large Rayleigh numbers ($Ra \sim 10^8$), small Ekman numbers ($Ek \sim 10^{-5} - 10^{-4}$) and small Rossby numbers ($Ro \sim 10^{-1}$). While this is generally consistent with the assumptions of the linear inviscid theory, Rossby numbers based on u_{max} were measured as high as 0.25 and probably would have exceeded this if not constrained by nonlinear momentum fluxes. The linear theory should therefore be regarded only as a limiting case.

3.1. *Surface flow*

The characteristics of the flow at the free surface were determined from photographic images and video recordings. Examples of streak photographs covering a range of conditions are shown in figure 5. They reveal strong azimuthal jets which narrowed and became more unstable as *Fr* increased, until multiple jets formed when $Fr \sim 10^2$. These types of images were used to measure the radial width of the azimuthal jets and their associated wave motions. Streak lengths and particle tracings from video recordings also provided quantitative information on the surface velocity field. Surface flow patterns were most clearly defined by video recordings of relatively wide jets. These revealed that slowly moving particles were first entrained on the deeper side of the jet. They were then accelerated azimuthally, while slowly migrating radially across the jet. After reaching a peak velocity, particles decelerated until they escaped from the shallow side of the jet where they were often entrained by cyclonic vorticies. Particles typically remained within the jet for between one and three rotation periods. The acceleration phase is qualitatively consistent with the angular momentum conserving flow analysed in § 2. However, the deceleration phase is more likely to be controlled by nonlinear cross-stream momentum fluxes as detailed below.

The surface velocity field was complicated by cyclonic vorticies and instability of the jets. However, the structure could be resolved within relatively broad jets. An example of measurements taken from a video recording of floating aluminium particles is shown in figure 6, along with the linear inviscid limit. Both are non-

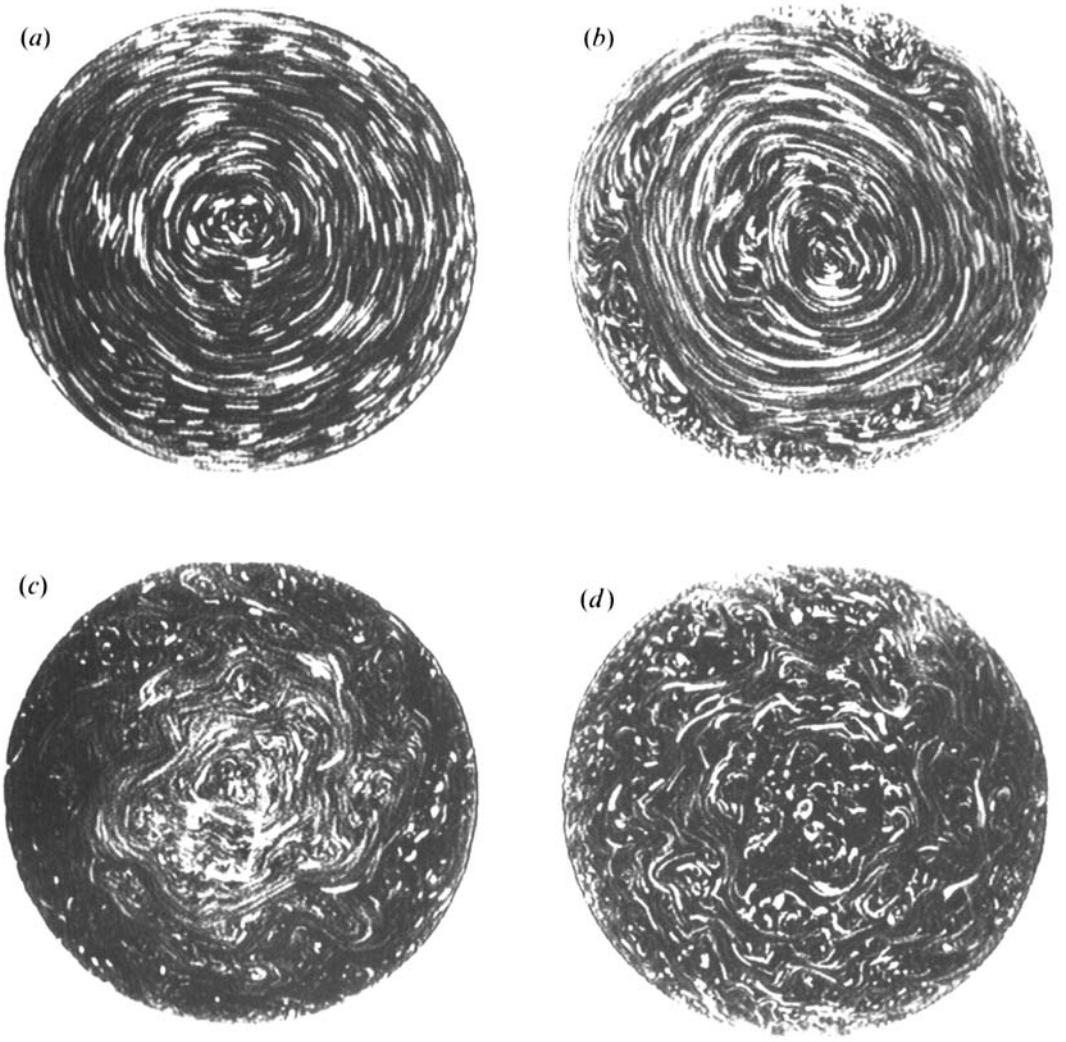

FIGURE 5. Streak photographs of flows driven by both bottom heating and surface cooling. The bowl dimensions are given in figure 2*b*. (*a*) $f = 0.5\ \mathrm{s}^{-1}$, $Ra = 2.0 \times 10^8$ and $Fr = 1.5$. (*b*) $f = 1.0\ \mathrm{s}^{-1}$, $Ra = 3.8 \times 10^8$ and $Fr = 3.2$. (*c*) $f = 2.0\ \mathrm{s}^{-1}$, $Ra = 2.8 \times 10^8$ and $Fr = 16.8$. (*d*) $f = 5.0\ \mathrm{s}^{-1}$, $Ra = 3.4 \times 10^8$ and $Fr = 78$. Vertical heat fluxes, based on relation (2.16) and constants given in Turner (1973), ranged from 0.7 $\mathrm{W\,cm}^{-2}$ for (*a*) to 1.6 $\mathrm{W\,cm}^{-2}$ for (*b*).

dimensionalized by the wave speed fR to give a Rossby number in accordance with the linear scaling (2.23). Initially the observed surface speed increases only marginally more slowly than the angular momentum conserving limit, but then falls off rapidly about midway across the jet. The small Ekman numbers associated with these flows indicate that molecular diffusion is not responsible for the observed flattening of the profile. A more likely candidate is the nonlinearity evident in figures 3 and 5. Cross-stream fluxes associated with nonlinear waves would reduce the acceleration on the deeper (anticyclonic) side of the jet and diffuse this momentum toward the shallow (cyclonic) side.

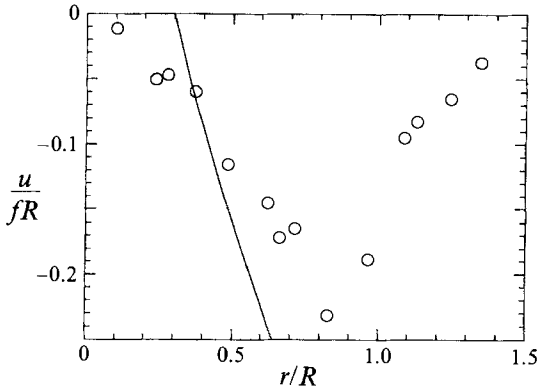

FIGURE 6. Radial distribution of non-dimensional azimuthal velocity for a flow heated from below with $f = 1.0\ \mathrm{s}^{-1}$, $Ra = 3.8 \times 10^8$ and $Fr = 3.2$ (○). This is compared with the linear limit assuming $r_1/R = 0.3$ (solid curve). In the absence of viscosity this limit would have infinite shear on the shallow side of the jet.

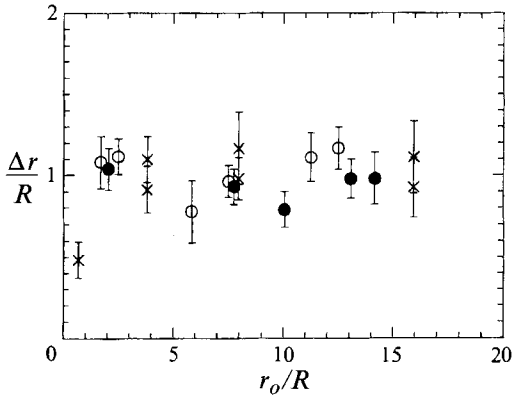

FIGURE 7. Non-dimensional cell width as a function of basin radius in units of R (i.e. $Fr^{1/2}$). Results are presented for all the configurations described in figure 2. The symbols correspond to the large insulated bowl (×), the small insulated bowl (•) and the small bowl with bottom heating (○).

While the detailed velocity structure is difficult to resolve in the more unstable jets, related flow characteristics such as the total jet width and maximum velocity could be determined over a wide parameter range. Streak photographs were used to take width measurements at eight evenly spaced locations along the jet circumference. Along any given radius, Δr was defined as the width of the zone of coherent azimuthal streaks, usually bounded by vorticies on either side. The mean width and its standard deviation are plotted for a range of conditions in figure 7. They have been non-dimensionalized by the deformation radius R in accordance with the linear scaling (2.20). The plot indicates that the cell width scales with R over most of the parameter range. This only breaks down when $Fr < 1$ and the width of the cell is influenced by the finite size of the bowl. The mean non-dimensional width of jets was $\Delta r/R = 1.01$, which is considerably larger than the corresponding linear inviscid estimates of $(2\gamma)^{1/2} = 0.24$ for narrow jets (equation (2.20)) and $2\gamma^{1/2} = 0.35$ for broad jets (equation (2.21)).

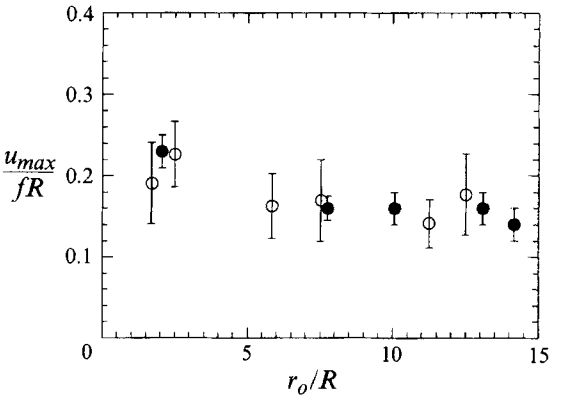

FIGURE 8. Non-dimensional maximum jet velocity as a function of basin radius in units of R (i.e. $Fr^{1/2}$). The symbols correspond to the small insulated bowl (•) and the small bowl with bottom heating (○).

This indicates that the broadening evident in figure 6 persists throughout the higher Froude number range.

Azimuthal speeds of the most rapidly moving particles in the jets could be best determined from video images. They are are plotted for a range of parameters in figure 8. Over most of this range the maximum non-dimensional speeds are marginally less than the linear estimate of $(2\gamma)^{1/2} = 0.24$ (equation (2.23)). The slightly higher speeds near $r_o/R = 1$ may be associated with the confinement of the bowl, which tends to suppress jet meanders and thus limit nonlinear fluxes. These results are again consistent with figure 6 and in combination with the total width measurements point to a significant nonlinear contribution for all $Fr \gg 1$.

The results of this section indicate that the linear limit provides an adequate description of the deeper (anticyclonic) side of the jet, while the shallower (cyclonic) side is dominated by nonlinear momentum fluxes. As a result, the total width scales very closely with the deformation radius R, without increasing the Rossby number beyond the linear limit of $(2\gamma)^{1/2}$. This is consistent with the numerical Hadley cell solutions of Schneider (1984), which suggest that nonlinear fluxes constrain Hadley cell jet velocities. Although we cannot measure these fluxes directly, figures 3 and 5 clearly demonstate that large-amplitude waves strongly perturb the jet motions. Experience suggests that this would be associated with substantial cross-stream diffusion of the jet's momentum.

Large-amplitude waves were first evident when $Fr \approx 2$ and became progressively more nonlinear as Fr increased. While some of the jet distortions were associated with the downwelling vorticies, more coherent wave forms are also evident. If these were due to baroclinic shear instability, then the wavenumber should scale with R^{-1}. This corresponds to a mode number (i.e. number of wave forms around the circumference of the jet) of $r_2/R = (r_2/r_o)Fr^{1/2}$. Reference to figure 5 (and other images not shown) confirms that this scaling agrees closely with experiment. This finding is consistent with the idea that the wave motions are responsible for the broadening of the jets. In particular, baroclinic instability operates by releasing the potential energy associated with the density field of the geostrophic flow and thus tends to induce cross-stream spreading.

3.2. *Temperature field*

Vertical and radial temperature profiles were recorded using a thermistor mounted on a traversing mechanism on the rotating table. Figure 9 shows examples of vertical profiles recorded near the mid radius of the bowl, with and without bottom heating. Temperature deviations from the mean have been non-dimensionalized in accordance with equation (2.19). This scaling is supported when ΔT is taken to be the mean temperature difference between the air and water for insulated flows and twice this figure for bottom heated flows which have two thermal boundary layers. Some of the temperature structure is associated with highly transient features; however, there are consistent underlying characteristics. All flows have an unstable near surface zone (superadiabatic), overlying a nearly neutral zone (adiabatic), and a deep stable zone (subadiabatic). At low rotation rates, nearly adiabatic conditions predominate. However, the depth of the superadiabatic and subadiabatic zones increases with f. Anomalously cold bottom water was only present when there was no bottom heating. Transient plumes can be identified by large temperature extremas in the fluid interior (figure 9*b*, profile ii). These were often encountered when profiles coincided with the non-hydrostatic region between two jets.

Figure 10 shows examples of horizontal temperature profiles for flows heated from below. Readings were taken across the diameter of the bowl at four depths. The depth dependence is consistent with the trends revealed by the vertical profiles. Within the horizontal structure, a high-wavenumber component is evident particularly near the surface where convective vortices were strongest. However, most of the structure in these and other profiles (not shown) scales with the deformation radius R. An individual cell can be identified by a drop in temperature with radius over this scale. The total drop across the bowl therefore increases with the number of cells present. A single cell fills most of the bowl in figure 10(*a*), while at least two cells are evident in figure 10(*b*). The profiles also confirm that the temperature drop across each cell scales as $\gamma\Delta T$. This provides further support that broadening of the cells beyond the linear limit is associated with wave processes, rather than any significant underestimation of the internal temperature differences (due for example to evaporative cooling).

The horizontal temperature structure within individual cells can be compared with the linear limit shown in figure 4. Since the horizontal temperature profiles at different depths were recorded sequentially rather than simultaneously, flow variability does not allow an accurate estimate of the depth-averaged temperature distribution. However, the radial gradients are quite consistent between profiles recorded away from the surface and bottom forcing, so reasonable comparisons can be made with individual profiles. Figure 11 shows the detailed temperature values over the width of cells from figure 10. These are compared with non-dimensionalized profiles calculated from linear theory (equation (2.12)). As with the surface velocity field, there is reasonable agreement on the deeper (anticyclonic) side of the cell. However, the nonlinear processes which transport momentum across the jets also carry heat and thereby weaken the temperature gradients on the shallow side.

In summary, the temperature data tend to support the general picture revealed by the surface flow field. That is, the velocity and density fields are governed mainly by linear angular momentum conserving dynamics on the deeper side of the jet. However, the shear on the shallow side is limited by baroclinic instability which drives nonlinear fluxes of momentum and heat. The net effect is a substantial broadening of the flow with corresponding reductions in the cross-stream velocity and temperature gradients.

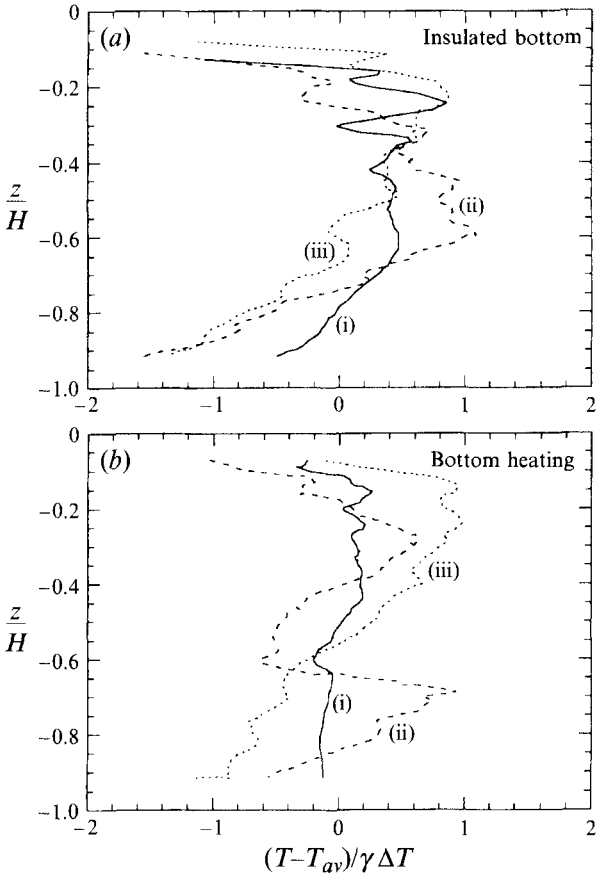

FIGURE 9. Vertical temperature profiles recorded at $r/r_o = 0.44$ in the two small bowls. T_{av} is the mean water temperature in the bowl. (*a*) Flows insulated below with (i) $f = 0.5\ s^{-1}$, $Ra = 9.8 \times 10^7$ and $Fr = 2.0$; (ii) $f = 2.0\ s^{-1}$, $Ra = 8.0 \times 10^7$ and $Fr = 36.0$; (iii) $f = 4.0\ s^{-1}$, $Ra = 8.2 \times 10^7$ and $Fr = 146$. (*b*) Flows heated from below with (i) $f = 0.5\ s^{-1}$, $Ra = 2.8 \times 10^8$ and $Fr = 0.61$; (ii) $f = 2.0\ s^{-1}$, $Ra = 2.8 \times 10^8$ and $Fr = 14.1$; (iii) $f = 4.0\ s^{-1}$, $Ra = 3.0 \times 10^8$ and $Fr = 37.0$.

3.3. *The influence of a solid upper boundary*

While the focus of the study is on free surface flows, a small number of experiments were conducted with a solid upper boundary for comparison. An example of the radial distribution of azimuthal velocity, recorded a few centimetres below the upper boundary using an LDV, is shown in figure 12. This reveals a single cell at least $4\dot{R}$ in width which fills most of the bowl. Motions near the outer edge of the bowl correspond to the lower part of the convection cell and are therefore expected to be in the opposing direction. Maximum non-dimensional velocities were typically an order of magnitude less than those recorded during free surface experiments. The slowing and broadening of the jet is consistent with the idea that much of the cross-isobath transport was carried in the Ekman layer. According to relation (2.26), the velocities in figure 12 correspond to a transport of $O(10^{-6}m^2s^{-1})$ within an Ekman layer of depth $O(10^{-3}m)$. The contrast between this and the free surface experiments clearly demonstrates the importance of the upper boundary condition.

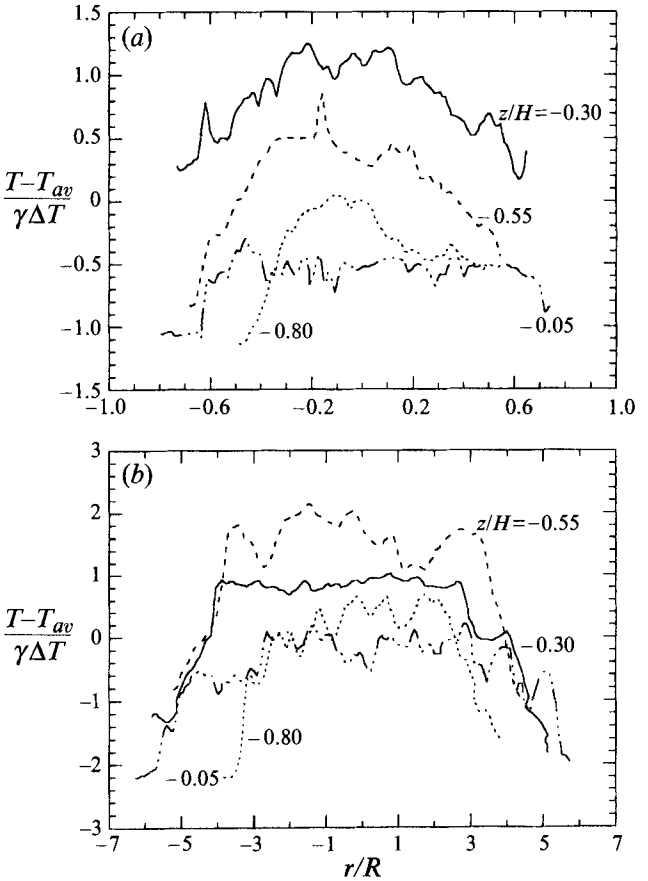

FIGURE 10. Horizontal temperature profiles at a number of depths for flows heated from below. T_{av} is the mean water temperature in the bowl. (*a*) A single cell fills most of the bowl with $f = 0.5\ \mathrm{s}^{-1}$, $Ra = 1.7 \times 10^8$ and $Fr = 0.60$. (*b*) Multiple cells with $f = 4.0\ \mathrm{s}^{-1}$, $Ra = 1.7 \times 10^8$ and $Fr = 39.6$.

3.4. *Flows with blocked isobaths*

In the axisymmetric bowl experiments all isobathic contours formed closed paths. In order to investigate the influence of blocked contours, a small number of experiments were also conducted in a rectangular container with a sloping bottom in one half. This system was rotated and cooled at the free surface, while the surface flow was again visualized using aluminium powder. A photograph of one of these flows is shown in figure 13. As expected, convective vorticies dominate the region where the bottom is flat. However, over the slope a topographic Hadley cell and its associated jet form parallel to the isobaths. This flow responds to blocking at the vertical boundaries by forming boundary currents which follow the perimeter of the container and close the horizontal circulation. The most intense boundary current flows toward the shallows. This is due to the propagation of energy in this direction by topographic Rossby waves over the slope.

This experiment also contrasts the different lengthscales associated with convective vortices and the eddies generated by baroclinic instability of mean horizontal flows. It has already been noted that convectively driven cyclonic vorticies dominate the flat bottomed region. However, much larger eddies with either cyclonic or anticyclonic

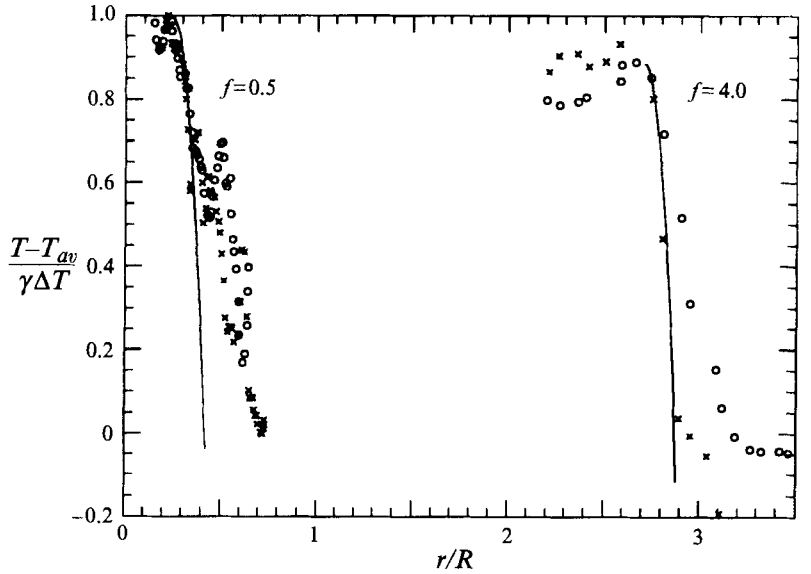

FIGURE 11. Detailed temperature data across individual laboratory cells. The data points are from the right (○) and mirror imaged from the left (×) of the $z/H = -0.30$ profiles in figure 10. They are compared with theoretical profiles (solid curve) based on the linear limit with $r_1/R = 0.035$ and $r_1/R = 2.7$.

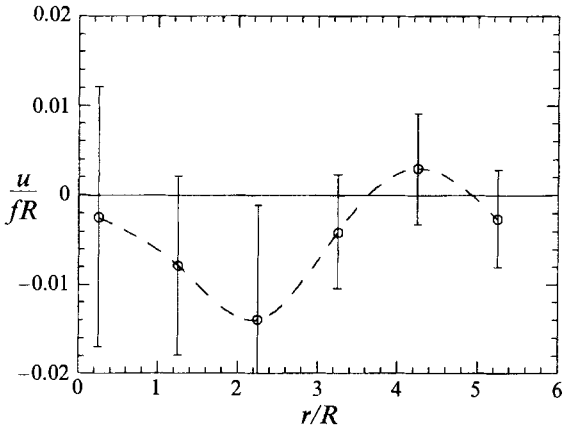

FIGURE 12. Radial distribution of non-dimensional azimuthal velocity for the flow beneath a rigid lid in the large insulated bowl with $f = 1.0\ s^{-1}$, $Ra = 5.1 \times 10^7$ and $Fr = 30.3$. Stationary readings were taken 3 cm below the lid over a 200 s period with a maximum sampling frequency of 15 s^{-1}. Mean values and one standard deviation in the natural variation of the signal are shown in the plot.

vorticity are also evident in figure 13. These develop from shear instabilities on both the Hadley cell jet and the boundary currents. The large amplitude of these waves compared to the axisymmetric flows suggests that reflection of energy at the blocked contours may have enhanced the wave growth.

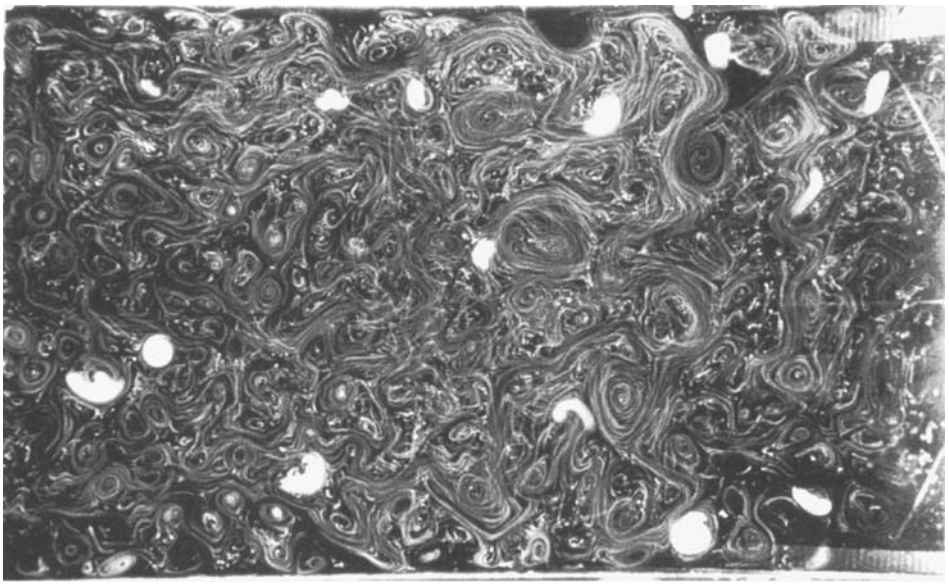

FIGURE 13. A streak photograph of surface cooled flow in a retangular tank (50 cm × 30 cm). The fluid depth was uniform ($H = 15$ cm) over the left-hand half of the tank, then decreased linearly to zero at the right-hand wall. The rotation rate corresponded to $f = 2.0\ \mathrm{s}^{-1}$ and the temperature difference between the air and water was 13°C.

4. Potential applications

The laboratory model may provide a useful analogue for a number of geophysical and astrophysical systems. In some of these systems, horizontal temperature gradients are generated by non-uniform heating rather than by topography. However, as noted in § 2, the essential features of the convection cell dynamics should be similar.

4.1. *Coastal seas*

Topographic Hadley cells may be important in continental shelf and slope seas, where surface cooling or evaporation drive convective overturning. They may be generated by either a sloping seafloor or non-uniform sea-surface buoyancy fluxes. Over a shelf region with typical parameters $f = 10^{-4}\ \mathrm{s}^{-1}$, $H = 100$ m and $\Delta\sigma = 10^{-3}$, equations (2.8) and (2.15) predict a maximum jet speed of $1.4\ \mathrm{m\,s}^{-1}$ and a cell width of 14 km. However, since nonlinear effects are also likely to influence coastal flows, these two figures should be regarded as upper and lower limits respectively.

In the northern hemisphere, surface jets associated with topographic Hadley cells would keep the coast to their left when looking in the downstream direction. They should therefore be easily distinguishable from surface flows driven by along-shelf density gradients, which keep the coast to their right. However, the structure of the cells may be complicated by wind stress, which often accompanies strong surface cooling. Opposing (downwelling) winds would tend to slow and broaden the surface jet as the cross-isobath transport is taken up by the wind-driven Ekman layer. In contrast, upwelling winds (same direction as the jet) generate Ekman transport which opposes the cross-isobath Hadley cell motion. This would result in narrow faster surface jets.

4.2. *Atmospheric Hadley cells*

A less direct analogy can also be drawn with large-scale convective motions in terrestrial and planetary atmospheres. In this role, the model topography is a convenient method for establishing radial temperature gradients. It also constrains barotropic radial motions and thus in a limited way provides an analogue for the planetary vorticity gradient. Topographic Hadley cells and their associated surface jets appear to be closely related to the atmospheric Hadley cells and the jet stream. The assumptions used in our theory are similar to those used in recent atmospheric models (Held & Hou 1980; Lindzen & Hou 1988) and the resulting flow patterns have many features in common. In particular, both flows are characterized by a non-hydrostatic convective region, which drives a relatively narrow hydrostatic jet along which baroclinic instabilities develop.

The analogy is of course limited by a number of factors. For example, radiative cooling is distributed over the full depth of the atmosphere and the latitudinal heating profile at the Earth's surface may be quite different from the corresponding radial laboratory profile. On the other hand, similarities between flows with and without bottom heating suggest that the main features of the flow are mainly determined by gross parameters such as the total available temperature differential. Perhaps a more important difference is the presence of first-order variations in the planetary vorticity over the width of the atmospheric Hadley cell. In particular, the topographic constraint in the laboratory model tends to be diminished by stratification and there is no means of including an equatorial region.

Despite these limitations, it can be argued that in many respects the model is more relevant to atmospheric Hadley cells than previous laboratory models, which utilized a solid upper boundary (Koschmieder & Lewis 1986; Miller & Fowlis 1986; Hathaway & Fowlis 1986). Most of the radial heat flux in these studies was concentrated within Ekman layers. Dissipation then allowed the convection cells to spread over the full radius of the container. The outer spherical boundary in the space-laboratory model of Hart, Glatzmaier & Toomre (1986) may have been similarly responsible for the equator to pole cells observed with meridional heating gradients. In contrast to these studies, the cell width in both our experiments and the real atmosphere is limited by the tendency to conserve angular momentum.

4.3. *Planetary atmospheres*

The absence of a planetary vorticity gradient in the model is perhaps less critical when applied to the atmospheres of the giant outer planets (Condie & Rhines 1994). The zonal jets on Jupiter and Saturn cover relatively narrow bands of latitude, the majority of which are outside the equatorial region. While there is still no concensus on the detailed dynamics of these flows, it is clear that the major driving force is the planets' interior heat (Pirraglia 1984).

The atmospheric interior of these planets can be divided into a subadiabatic region, extending from the cloud tops up to the tropopause, and a deeper convective region. Previous laboratory and numerical models have tended to focus on the subadiabatic region where quasi-geostrophic scaling may be applied (Read & Hide 1984; Read 1986; Sommeria, Meyers & Swinney 1988; Marcus 1988). Velocities in this region decrease with altitude, suggesting that they are driven by momentum transfer from the convectively driven jets below (Ingersoll *et al.* 1984). Flasar (1986) noted that the velocity distribution at the top of these jets can be reproduced by angular momentum conserving transport from lower to higher latitudes, followed by dissipation which reduces M to its local planetary value. This suggests that the flow may consist of

a series of convectively driven Hadley cells, with dissipation occurring in the strong upwelling (or downwelling) zones at the outer edges of the cells.

The major uncertainty in applying the model results is the penetration depth of the convection cells (Condie & Rhines 1994). Large depths comparable to the jet widths result in columnar convection patterns as first suggested by Busse (1976). However, the model provides realistic estimates of observable quantities when shallower depths, comparable to the scale height $O(100$ km) are assumed. For example, utilizing a value of $\Delta\sigma\overline{H} = 1.2$ km for Jupiter (Ingersoll & Cuzzi 1969), yields a cell width of $O(10^4$ km) and a maximum jet velocity of $O(10^2$ m s^{-1}).

5. Conclusion

Topographic Hadley cells have been analysed in the linear limit under assumptions of hydrostatic flow, geostrophy and inviscid surface flow which conserves angular momentum. This yields the following scales for the width and maximum azimuthal velocity of the hydrostatic region of the cell:

$$\Delta r = c_1 \gamma^{1/2} R, \tag{5.1}$$

$$u_{max} = c_2 \gamma^{1/2} f R, \tag{5.2}$$

where c_1 and c_2 are dimensionless constants. In the linear limit $c_1 = c_2 = \sqrt{2}$ for jets which are narrow compared with their path radius, while $c_1 = 2$ and $c_2 = 1$ for jets in which these two quantities are comparable. The laboratory experiments yield similar temperature and velocity profiles on the deep side of the jets. However, these flows are baroclinically unstable and large-amplitude meanders broaden the jets and reduce the shear, particularly on the shallow side. This observation is consistent with related numerical solutions (Schneider 1984; Held & Hou 1980). The broadening trend is most prevalent in experiments characterized by large Froude numbers, where wave growth is not impeded by the proximity of the outer boundary of the bowl. However, even under these circumstances the *total* width of the jets continues to scale with the deformation radius with constants of $c_1 = 5.8 \pm 1.2$ and $c_2 = 0.92 \pm 0.11$.

S.A.C. was supported by a fellowship from the University Corporation for Atmospheric Research (UCAR). A number of the laboratory experiments were conducted at the Australian National University.

Appendix. Conditions for cell generation

To understand the conditions under which topographic Hadley cells might develop, consider again the system shown in figure 1. With no along-isobath gradients, the depth-averaged heat equation can be written

$$\frac{\partial T}{\partial t} + \frac{\partial}{\partial r}(\overline{u_r T}) = \kappa \frac{\partial^2 T}{\partial r^2} - \frac{Q}{\rho c_p H}, \tag{A 1}$$

where c_p is the specific heat, u_r is the radial velocity and $\overline{u_r T}$ is the depth-averaged radial heat transport associated with the Hadley cell. The radial transport associated with turbulent processes, such as convective vortices, is conveniently characterized by a diffusivity κ. If there is no Hadley cell we can write

$$\frac{\partial}{\partial t}(T_1 - T_2) = \kappa \frac{\partial^2}{\partial r^2}(T_1 - T_2) - \frac{Q}{\rho c_p}\left(\frac{1}{H_1} - \frac{1}{H_2}\right), \tag{A 2}$$

where the subscripts refer to any two radii. If the flow is quasi-steady so that $T_1 - T_2$ is independent of time, we are left with a balance between surface cooling and horizontal diffusion. However, if the heat flux term exceeds the diffusion term, then the advective term must make a contribution through the formation of a Hadley cell. The condition for cell formation can therefore be written in scaled form as

$$Q > \frac{\rho c_p \kappa H^2 \Delta\sigma}{\alpha\beta\Delta r^3}, \tag{A 3}$$

where $\beta = (H_1 - H_2)/\Delta r$ is the characteristic slope of the topography. Substituting (2.19)–(2.22) this becomes

$$Q > \frac{\rho c_p \kappa f^3}{\beta} \left\{ \frac{H}{g^3\alpha^3\gamma\Delta T} \right\}^{1/2}. \tag{A 4}$$

This result has little predictive power since the use of simple diffusion may not be appropriate and κ is in any case poorly constrained. However, its functional form provides insight into the influence of the various parameters. In particular, a cell is unlikely to form in a very deep region or where the slope is very gentle. In both cases, significant horizontal temperature gradients cannot develop from uniform surface cooling. Another interesting aspect is that rotation tends to inhibit cell formation by restricting the cross-slope distance over which the required horizontal temperature difference must develop.

REFERENCES

BOUBNOV, B. M. & GOLITSYN, G. S. 1986 Experimental study of convective structures in rotating fluids. *J. Fluid Mech.* **167**, 503–531.

BUSSE, F. H. 1976 Experimental study of convective structures in rotating fluids. *Icarus* **29**, 255–260.

CHANDRASEKHAR, S. 1961 *Hydrodynamic and Hydromagnetic Stability*. Oxford University Press.

CHEN, R., FERNANDO, H. J. S. & BOYER, D. L. 1989 Formation of isolated vortices in a rotating convecting fluid. *J. Geophys. Res.* **94**, 18445–18453.

CONDIE, S. A. & RHINES, P. B. 1994 A convective model for the zonal jets in the atmospheres of Jupiter and Saturn. *Nature* **367**, 711–713.

FERNANDO, H. J. S., CHEN, R. & BOYER, D. L. 1991 Effects of rotation on convective turbulence. *J. Fluid Mech.* **228**, 513–547.

FLASAR, F. M. 1986 Global dynamics and thermal structure of Jupiter's atmosphere. *Icarus* **65**, 280–303.

HART, J. E., GLATZMAIER, G. A. & TOOMRE, J. 1986 Space-laboratory and numerical simulations of thermal convection in a rotating hemispherical shell with radial gravity. *J. Fluid Mech.* **173**, 519–544.

HATHAWAY, D. H. & FOWLIS, W. W. 1986 Flow regimes in a shallow rotating cylindrical annulus with temperature gradients imposed on the horizontal boundaries. *J. Fluid Mech.* **172**, 401–418.

HELD, I. M. & HOU, A. Y. 1980 Nonlinear axially symmetric circulations in a nearly inviscid atmosphere. *J. Atmos. Sci.* **37**, 515–533.

INGERSOLL, A. P., BEEBE, R. F., CONRATH, B. J. & HUNT, G. E. 1984 Structure and dynamics of Saturn's atmosphere. In *Saturn* (ed. T. Gehrels & M. S. Matthews), pp. 195–238. The University of Arizona Press.

INGERSOLL, A. P. & CUZZI, J. N. 1969 Dynamics of Jupiter's cloud bands. *J. Atmos. Sci.* **26**, 981–985.

KOSCHMIEDER, E. L. & LEWIS, E. R. 1986 Hadley circulations on a nonuniformly heated rotating plate. *J. Atmos. Sci.* **43**, 2514–2526.

LINDZEN, R. S. & HOU, A. Y. 1988 Hadley circulations for zonally averaged heating centered off the equator. *J. Atmos. Sci.* **45**, 2416–2427.

MARCUS, P. S. 1988 A numerical simulation of the Great Red Spot of Jupiter. *Nature* **331**, 693–696.

MILLER, T. L. & FOWLIS, W. W. 1986 Laboratory experiments in a baroclinic annulus with heating and cooling on the horizontal boundaries. *Geophys. Astrophys. Fluid Dyn.* **34**, 283–300.

NAKAGAWA, Y. & FRENZEN, P. 1955 A theoretical and experimental study of cellular convection in rotating fluids. *Tellus* **7**, 1–21.

PEDLOSKY, J. 1987 *Geophysical Fluid Dynamics.* Springer-Verlag.

PIRRAGLIA, J. A. 1984 Meridional energy balance of Jupiter. *Icarus* **59**, 169–176.

READ, P. L. 1986 Stable, baroclinic eddies on Jupiter and Saturn: A laboratory analog and some observational tests. *Icarus* **65**, 304–334.

READ, P. L. & HIDE, R. 1984 An isolated baroclinic eddy as a laboratory analogue of the Great Red Spot on Jupiter. *Nature* **308**, 45–48.

SCHNEIDER, E. K. 1984 Response of the annual and zonal mean winds and temperatures to variations in the heat and momentum sources. *J. Atmos. Sci.* **41**, 1093–1115.

SOMMERIA, J., MEYERS, S. D. & SWINNEY, H. L. 1988 Laboratory simulation of Jupiter's Great Red Spot. *Nature* **331**, 689–693.

TURNER, J. S. 1973 *Buoyancy Effects in Fluids.* Cambridge University Press.